








Cite this: *J. Mater. Chem. A*, 2022, 10, 12177

Study of thermal material properties for Ta- and Al-substituted $\text{Li}_7\text{La}_3\text{Zr}_2\text{O}_{12}$ (LLZO) solid-state electrolyte in dependency of temperature and grain size†

Julian Neises, ^{*a} Walter Sebastian Scheld, ^b Ah-Ram Seok, ^b Sandra Lobe, ^b Martin Finsterbusch, ^{bc} Sven Uhlenbruck, ^{bc} Roland Schmechel ^a and Niels Benson ^{*a}

Solid-state electrolytes such as tantalum (Ta)- and aluminum (Al)-substituted $\text{Li}_7\text{La}_3\text{Zr}_2\text{O}_{12}$ (LLZO) are seen as the key component for the next generation of mainstream battery technology. However, this development often lacks specific information on decisive material parameters. Therefore, this work experimentally investigates the thermal material parameters such as the thermal conductivity (κ) and the specific heat capacity (C_p) of LLZO between room temperature and 1225 K using laser flash analysis (LFA) and differential scanning calorimetry (DSC). The DSC measurements reveal a C_p of 0.55–0.80 J g^{−1} K^{−1}. Furthermore, a decomposition of the cubic LLZO phase to pyrochlore $\text{La}_2\text{Zr}_2\text{O}_7$ is detected between 1500 K and 1750 K, which is substantiated by Raman- and SEM-analysis. The impact of the grain size on κ is also considered, as the Al-substitution leads to the formation of significantly larger grain sizes compared to a Ta-substitution. The LFA measurements yield a relatively constant κ between 1.45–1.55 W m^{−1} K^{−1} for both materials and grain sizes, which is the consequence of a phonon mean free path in the range of the interatomic distance of the LLZO crystal. This implies that phonon scattering at grain boundaries is negligible and the main scattering occurs at inhomogeneities in the crystal lattice.

Received 13th January 2022
Accepted 19th May 2022

DOI: 10.1039/d2ta00323f

rsc.li/materials-a

1 Introduction

All-solid-state batteries are considered a potential candidate for the next generation of mainstream battery technology, as they offer higher operational safety, larger energy densities, and potentially faster charging when compared to conventional lithium (Li)-ion batteries.¹ Research has shown that garnet-based Li-oxides exhibit the required high ionic conductivity, as well as good chemical stability against possible electrode materials.^{1–4} Especially the solid electrolyte with the nominal formula $\text{Li}_7\text{La}_3\text{Zr}_2\text{O}_{12}$ (LLZO) has been extensively studied due to its high Li^+ conductivity ($\sigma_{\text{Li}} > 10^{-4}$ S cm^{−1}) at room temperature (RT) and stability in conjunction with Li metal anodes.¹ LLZO possesses a cubic phase which crystallizes in the space group $Ia\bar{3}d$ and a tetragonal phase ($I4_1/acd$).^{1,5,6} The tetragonal phase shows a higher-ordered arrangement of Li^+ compared to the cubic crystal phase.⁶ The distorted

arrangement of Li^+ in the cubic crystal phase leads to two orders of magnitude higher Li^+ conductivity.^{1,5,6} The tetragonal phase, which is the thermodynamically stable phase at ambient conditions, undergoes a phase transition to cubic between 100 °C and 150 °C.^{5,7,8} It has been reported that doping the LLZO with elements such as Al,^{5,9,10} Ga,^{9,11} Ta,^{9,12–14} or Nb¹⁵ stabilizes the cubic crystal phase at room temperature after sintering at high temperatures ($T > 1000$ °C). Doping with such super valent cations leads to a decrease in Li content by forming Li site vacancies, in order to restore electro-neutrality. The substitution cations can either reside on the Li site, *e.g.* $\text{M} = \text{Al}$ or Ga ($\text{Li}_{7-3x}\text{M}_x\text{La}_3\text{Zr}_2\text{O}_{12}$) creating two Li vacancies per substitution or on the Zr site, *e.g.* $\text{M} = \text{Ta}$ or Nb ($\text{Li}_{7-y}\text{La}_3\text{Zr}_{2-y}\text{M}_y\text{O}_{12}$) which creates one vacancy for each substitution. The critical level of Li site vacancies to stabilize the cubic phase was experimentally found to be 0.2–0.6 mol per LLZO formula unit.^{9,12,16,17}

Besides the need for the cubic crystal phase to attain high Li^+ conductivity, a dense microstructure is required which also reduces the grain boundary resistance.¹⁸ In order to achieve highly dense materials, various methods have been investigated, such as long-term sintering at high temperatures of isostatic cold-pressed pellets,^{1,5} hot-pressing,^{9,11} or the usage of sintering aids.^{19–22} For all of these methods, the thermal budget of the LLZO must not be exceeded as this would lead to Li loss

^aInstitute of Technology for Nanostructures (NST), University Duisburg-Essen, 47057 Duisburg, Germany. E-mail: niels.benson@uni-due.de^bInstitute of Energy and Climate Research – Materials Synthesis and Processing (IEK-1), Forschungszentrum Juelich GmbH, 52425 Juelich, Germany^cHelmholtz Institute Muenster, Wilhelm-Johnen Str., 52425 Juelich, Germany† Electronic supplementary information (ESI) available. See <https://doi.org/10.1039/d2ta00323f>

and finally to the decomposition of the cubic LLZO phase.^{23,24} Even though this garnet-based solid electrolyte has attracted a lot of scientific attention in the last decade, its thermal material parameters such as thermal conductivity and specific heat capacity are often unknown. Their knowledge could lead to a better understanding of thermal processes in LLZO, especially regarding computational simulations of such thermal treatments²⁵ or heat distributions in battery cells²⁶ where they are crucial input parameters.

The present study therefore experimentally determines the temperature-dependent thermal conductivity of cubic LLZO using laser flash analysis (LFA). Simultaneous thermal analysis (STA) is applied to determine the temperature dependence of the specific heat capacity, as well as the decomposition temperature of cubic LLZO. The latter is verified by Raman spectroscopy and SEM measurements. Furthermore, the influence of the grain size on the thermal conductivity is discussed by comparing two differently substituted LLZO's (Ta or Al) with clearly different grain sizes.

2 Experimental

Ta-substituted LLZO (LLZO:Ta), nominally without any addition of Al, and Al-substituted LLZO (LLZO:Al, $\text{Li}_{6.4}\text{Al}_{0.2}\text{La}_3\text{Zr}_{1.6}\text{O}_{12}$) powder were synthesized *via* a standard solid-state reaction route. Al diffused from the alumina crucible into LLZO:Ta during the sintering step which led to an equivalent composition of $\text{Li}_{6.45}\text{Al}_{0.05}\text{La}_3\text{Zr}_{1.6}\text{Ta}_{0.4}\text{O}_{12}$. The prepared powder was calcinated at 850 °C and 1000 °C in several steps. The material was sintered in a rod at 1175 °C for four hours in air and cut with a low-speed saw (Buehler IsoMet™) in pellets with the required thickness. The preparation process followed the method described by Tsai *et al.* and can be found in detail in the corresponding publications.^{27,28}

The grain size of the samples was determined by scanning electron microscope (SEM) analysis. Prior to measurement, the samples were prepared *via* a thermal etching process to enhance grain boundary grooving.^{29,30} For this purpose, the samples were polished with 4000 grit sandpaper and then heated to 1100 °C with a heating rate of 10 K min⁻¹. SEM measurements were performed after cooling. The obtained SEM images were then analyzed with the software ImageJ (version 1.52a) in order to measure the diameter of the visible grains. Despite the fact that SEM analyses of polished and thermally etched surfaces lead to an underestimation of the real grain size, due to the presence of irregular transgranular cuts,³⁰ this method is sufficient to compare the grain size of the examined LLZO:Ta and LLZO:Al.

The crystal phase of the samples was determined by X-ray diffraction (XRD) in air, using a Bruker D 4 Endeavor device with Cu K α radiation. Measurements were done with sintered pellets of LLZO:Ta and LLZO:Al between $2\theta = 10\text{--}80^\circ$ with the Bragg–Brentano geometry. A Rietveld refinement of the measured diffractograms was performed with the software MAUD (version 2.98)^{31,32} using reference phase data of cubic LLZO from the inorganic crystal structure database (ICSD, $\text{Li}_7\text{La}_3\text{Zr}_2\text{O}_{12}$ #422259).

Measurements of the ionic conductivity were done by electrochemical impedance spectroscopy (EIS) at room temperature with a Biologic VMP-300 from 1 Hz to 7 MHz. Au was sputtered on the samples as a blocking electrode. The measured impedance spectra were analyzed by ZView software.

Raman measurements to evaluate the structural phases of sintered LLZO:Ta and LLZO:Al pellets were carried out in air with a Renishaw InVia Raman microscope in backscattering geometry using a solid-state 532 nm excitation laser and an 1800 l mm⁻¹ grating. The laser power was set to 0.39 mW in order to prevent laser-induced sample damage during the measurement. A 100 \times objective was chosen, resulting in a laser spot diameter of $\sim 1\text{ }\mu\text{m}$.

Simultaneous thermal analysis (STA), which combines differential scanning calorimetry (DSC) and thermogravimetry (TG) were carried out with a NETZSCH STA 449 F5 Jupiter in order to investigate the specific heat capacity (C_p) and decomposition temperature of sintered LLZO:Ta. Sintered LLZO:Ta powder was pressed into a pellet (5 mm diameter) with a uniaxial pressure of 15 kN for 15 min, resulting in a relative density of 55%. The pressed pellet was placed into a Pt crucible with a perforated lid. A connected quadrupole mass spectrometer (QMS, NETZSCH QMS 403 Aeolos Quadro) enables for analysis of evaporated species. Two continuous heating steps were conducted in an argon (Ar) atmosphere (70 ml min⁻¹). During the first heating step, to analyze evaporated species, a heating rate of 20 K min⁻¹ was applied to heat the sample from room temperature (RT) to 1273 K. After cooling down to room temperature again, the sample was heated to 1773 K with 20 K min⁻¹ in the second heating step, to determine the specific heat capacity (C_p ; with index p indicating constant pressure), using a sapphire reference following the method described by O'Neill.³³

Laser flash measurements were performed with a NETZSCH LFA 457 MicroFlash to assess the temperature-dependent thermal conductivity of LLZO:Ta and LLZO:Al and to investigate the influence of the grain size on this material parameter. The sintered pellets, with a diameter of approximately 10 mm and a thickness of 1.7–2.0 mm were heated for three hours at 1073 K in an Ar-atmosphere before the measurement to remove surface lithium carbonate (Li_2CO_3). The samples were then coated with graphite on both surfaces to improve their absorption/emission characteristic. Measurements were done within a temperature range from RT to 1225 K in temperature steps of 100 K. The thermal conductivity was calculated employing the procedure introduced by Parker *et al.*³⁴ using a transparent (radiation) model in the analyzation software provided by the LFA manufacturer (NETZSCH LFA Analysis version 7.1.0).³⁵ The measurements were carried out in a reducing argon/hydrogen (5% H₂ in Ar) atmosphere (purge flow of 75 ml min⁻¹) in order to prevent a reaction at elevated temperatures between LLZO, the necessary graphite coating for the LFA measurement and any remaining oxygen in the system. In a technical argon atmosphere (purity grade 4.9), which always contain an amount of oxygen and water, the graphite coating disappeared completely when heating up to 973 K. This led to a partial transmission of the laser flash through the



sample so that the LFA signals could not be evaluated anymore. This phenomenon indicates the reaction of LLZO with graphite and oxygen forming lithium carbonate (Li_2CO_3) at the sample surface, which starts to melt between 925–973 K (compare DSC measurement in Fig. 3a).

3 Results and discussion

3.1 Grain size and density

The grain size of LLZO:Ta and LLZO:Al was determined using SEM analysis of thermally etched samples (Fig. 1a and b). The analysis revealed D10, D50, and D90 percentile values of 5.8 μm , 11.6 μm , and 18.6 μm for LLZO:Ta and 284.2 μm , 512.5 μm , and 909.3 μm for LLZO:Al (see Fig. S1 in ESI†). The true grain size is thought to be slightly larger than the measured grain size, as the cross-section cuts randomly through the grains and the sizing of the visible transgranular cuts leads to the grains size being systematically measured too small.³⁰ However, the analysis revealed clearly different grain sizes for LLZO:Ta and LLZO:Al. The larger grain size for the Al-substituted LLZO, despite both materials being synthesized *via* the same reaction route and with the same temperature treatment, is attributed to aluminum as substitution cation, which is known to be a sintering aid enhancing grain growth.^{28,36} The effective density (ρ_{eff}) was geometrically determined to 4.62 g cm^{-3} for LLZO:Ta and 4.68 g cm^{-3} for LLZO:Al.

3.2 X-ray diffraction

The diffractograms for Al- and Ta-substituted LLZO correspond well with the cubic garnet-phase $\text{Li}_7\text{La}_3\text{Zr}_2\text{O}_{12}$ (ICSD #422259)³⁷

with space group $Ia\bar{3}d$. The Rietveld refinement with the software MAUD reveals no side phases or impurities in the diffractograms (Fig. 2). It converges for LLZO:Al to $R_{\text{wp}} = 8.08\%$, $R_{\text{exp}} = 2.98\%$, $\chi^2 = R_{\text{wp}}/R_{\text{exp}} = 2.71$ and results in a lattice constant of $a = 12.950 \text{ \AA}$. The final R -values for LLZO:Ta are $R_{\text{wp}} = 10.31\%$, $R_{\text{exp}} = 2.95\%$, $\chi^2 = 3.61$ and the lattice constant refines to $a = 12.943 \text{ \AA}$. The refined lattice constants correspond well with reported results in the literature for LLZO:Al ($a = 12.957 \text{ \AA}$ (ref. 38)) and LLZO:Ta ($a = 12.945\text{--}12.948 \text{ \AA}$ (ref. 12, 14 and 38)). Both substitutions cause a slight decrease of the lattice parameter compared to unsubstituted cubic LLZO ($a = 12.968 \text{ \AA}$ (ref. 1) and $a = 12.983 \text{ \AA}$ (ref. 37)). This decrease can be explained by a lattice shrinkage, as the ionic radii of the substitution ions Ta^{5+} (0.64 \AA) and Al^{3+} (0.53 \AA) are smaller than that of the respectively replaced ions Zr^{4+} (0.72 \AA) and Li^+ (0.76 \AA).^{39–41}

The refined lattice parameters can be used to calculate the theoretical density ρ_{theo} of the investigated material using the following formula:

$$\rho_{\text{theo}} = \frac{ZM}{N_A a^3} \quad (1)$$

With Z being the number of formula units in the unit cell, M the molar mass, N_A the Avogadro constant ($6.022 \times 10^{23} \text{ mol}^{-1}$), and a the lattice constant. The respective parameters for LLZO:Al and LLZO:Ta are shown in Table 1. The comparison of the theoretical density (ρ_{theo}) with the measured effective density (ρ_{eff}) of the sintered sample pellets leads to a relative density (ρ_{rel}) of 91% for LLZO:Al and 86% for LLZO:Ta.

3.3 Electrical properties

EIS measurements were conducted at RT to determine the ionic conductivity of LLZO:Ta and LLZO:Al (see Fig. S2 in ESI†). The total ionic conductivity was calculated to 0.696 mS cm^{-1} for LLZO:Ta and 0.370 mS cm^{-1} for LLZO:Al which is comparable to other reported LLZO with similar substitutions.^{9,12,28,42,43}

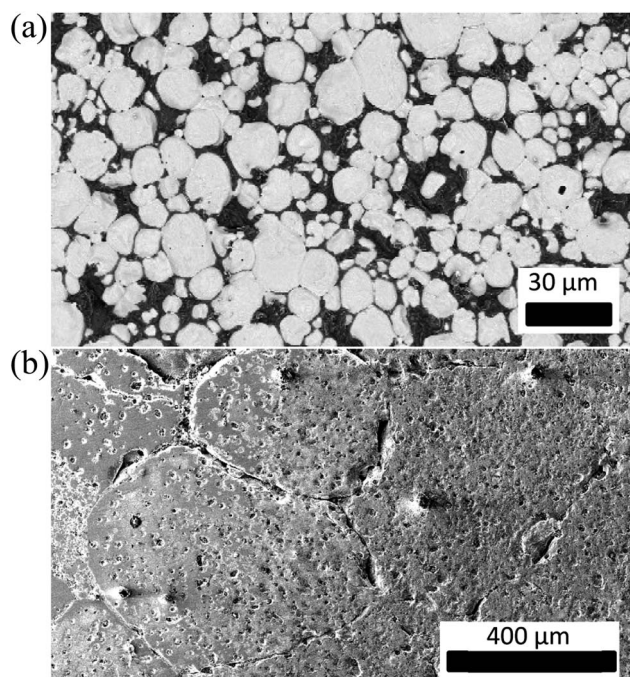


Fig. 1 Top view scanning electron microscope (SEM) images of thermally etched samples of (a) LLZO:Ta and (b) LLZO:Al (10 kV acceleration voltage).

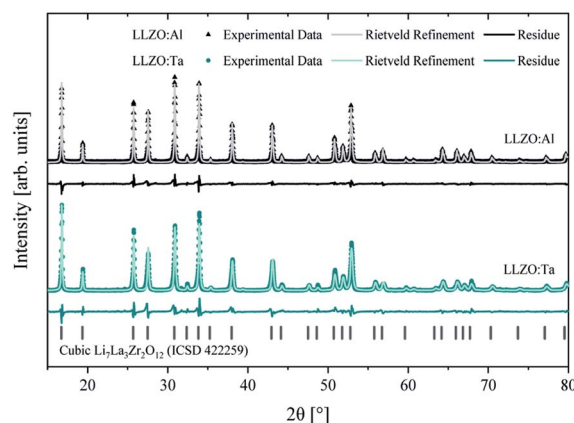


Fig. 2 X-ray diffraction pattern of Al- and Ta-substituted LLZO phase. Data are refined with the Rietveld method. The vertical lines indicate the Bragg reflection positions of cubic garnet-phase $\text{Li}_7\text{La}_3\text{Zr}_2\text{O}_{12}$ (ICSD #422259) with space group $Ia\bar{3}d$.



Table 1 Parameters for LLZO:Al and LLZO:Ta to calculate the theoretical density ρ_{theo} with a the lattice constant derived from XRD measurements, M the molar mass calculated from the molecular formula, Z the number of formula units in the unit cell, ρ_{eff} the measured effective density of the sintered sample and ρ_{rel} the resulting relative density

Material	LLZO:Ta	LLZO:Al
a [Å]	12.943	12.950
M [g mol ⁻¹]	973.16	840.97
Z	8	8
ρ_{theo} [g cm ⁻³]	5.35	5.15
ρ_{eff} [g cm ⁻³]	4.62	4.68
ρ_{rel} [%]	86	91

3.4 Simultaneous thermal analysis

As the calculation of the C_p requires a constant sample mass, a pre-heating step up to 1270 K was applied to the sample prior to the actual measurement, in order to evaporate thermally unstable components (Fig. 3a).

Three separate mass loss steps can be identified, resulting in a total mass loss of -2.4% . The first mass loss step of -1.7% between 470 K and 700 K, along with an endothermic peak at 600 K, can be ascribed to the evaporation of H_2O molecules inserted in the garnet structure.⁴⁴ Here, a quadrupole mass spectrometer (QMS) was used to quantify the evaporation of H_2O ($m/z = 18$), which is shown in Fig. 3b. A quantitative assessment of the evaporated water is difficult, as it is influenced by condensation in the DSC equipment and therefore numbers might differ between different nominally identical experiments. The second endothermic peak at 690 K with a subsequent mass loss of -0.2% at 770 K and the emission of H_2O ($m/z = 18$) are suggested to be associated with the melting and decomposition of LiOH .⁴⁵ The third endothermic peak at 973 K without a mass loss can be assigned to the melting of Li_2CO_3 , present at the LLZO:Ta surface.^{46,47} The third mass loss step of -0.5% between 1000 K and 1200 K accompanied with a broad endothermic peak in the DSC signal centered at 1157 K is caused by the decomposition of Li_2CO_3 ,^{24,46,48} which results in the emission of CO_2 ($m/z = 44$), as detected by QMS analysis (Fig. 3b). No further weight loss is found beyond 1200 K.

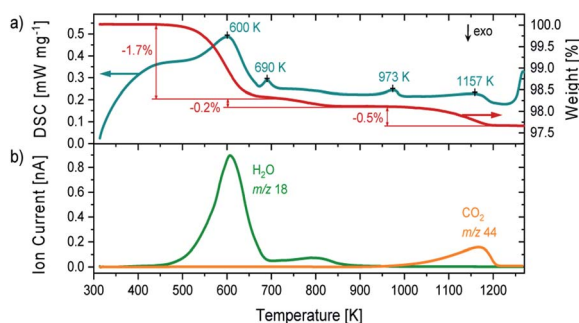


Fig. 3 (a) Differential scanning calorimetry (DSC) and thermogravimetric (TG) measurements of sintered LLZO:Ta powder upon first heating after exposure to air; (b) with the relative mass spectrum of H_2O ($m/z = 18$) and CO_2 ($m/z = 44$).

The STA analysis of sintered LLZO:Ta powder suggests the presence of LiOH and Li_2CO_3 on the LLZO surface.^{49,50} Here, Xia *et al.*⁴⁹ proposed a three-stage mechanism at the LLZO surface upon air exposure: (i) water vapor is adsorbed to sample surface; (ii) Li^+/H^+ exchange occurs to form $\text{LiOH} \cdot \text{H}_2\text{O}$ and hydrated LLZO; and (iii) $\text{LiOH} \cdot \text{H}_2\text{O}$ reacts with CO_2 to form Li_2CO_3 . During heating, the reaction would take place in reverse order.⁴⁴

The consecutive heating step up to 1780 K for the actual C_p evaluation of the LLZO:Ta sample results in only a minor mass loss of -0.1% above 1600 K. The constant mass below 1600 K allows for calculating the specific heat capacity C_p of the LLZO:Ta sample (Fig. 4). As C_p is not defined during any phase transitions, such as centered at 1266 K and 1694 K, the derived C_p is only valid for $T < 1225$ K (inset in Fig. 4). The large endothermic peak centered at 1694 K, is interpreted as the decomposition of the cubic LLZO crystal phase which starts at 1500 K. The determined decomposition enthalpy is 463.5 J g^{-1} . This decomposition was further investigated with Raman and SEM analysis in the following section. The origin of the minor endothermic event at 1266 K with an enthalpy of 12.4 J g^{-1} is still unclear. However, none of the present components show a common phase transition at this temperature and this peak is not present in comparable measurements with LLZO:Al. Consequently, it can be concluded that this endothermic event does not originate from a Li-Al side phase and it could be an indication that it is related to the tantalum substitution of LLZO. Hwang *et al.*⁵¹ report the reduction of tantalum oxide (Ta_2O_5) in the presence of magnesium gas, as a reducing agent, for a temperature range of 1173–1223 K. Therefore, the endothermic peak at 1266 K could be related to a partial reduction of Ta_2O_5 in a lithium enriched atmosphere under the prevailing experimental conditions.

The specific heat capacity C_p of LLZO:Ta increases from $0.544 \text{ J g}^{-1} \text{ K}^{-1}$ at 300 K to $0.771 \text{ J g}^{-1} \text{ K}^{-1}$ at 1225 K (inset Fig. 4). The temperature dependence of C_p can be expressed with the following equation in the often used polynomial form⁵² (dashed black line in inset Fig. 4):

$$C_p(T) = a + bT + cT^{-2} \quad (2)$$

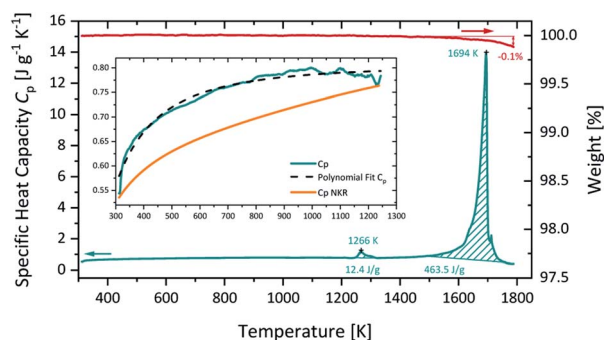


Fig. 4 Thermogravimetric (TG) curve (red) and the derived temperature-dependent specific heat capacity (C_p , cyan) of sintered LLZO:Ta from a DSC measurement in Ar-atmosphere. Inset: closeup to C_p in a temperature range from 300–1225 K with a polynomial fit (eqn (2)).

which yields the specific heat capacity C_p in $\text{J g}^{-1} \text{K}^{-1}$, with T the temperature in K and the polynomial coefficients $a = 0.81$, $b = 2.27 \times 10^{-6}$ and $c = 2.24 \times 10^4$.

A theoretical estimation of the molar heat capacity ($C_{p,m}$) can be done by the Neumann–Kopp rule (NKR). In its primary form, it describes the molar heat capacity of a compound as the, by mass fraction weighted sum of the heat capacities of its components.⁵³ More accurate results can be obtained for binary compounds in a complex form, whereas the heat capacity of complex compounds can be calculated as follows:^{54–57}

$$C_{p,m}(\text{CO}) = \sum n(\text{BO}) C_{p,m}(\text{BO}) \quad (3)$$

where $C_{p,m}$ is the molar heat capacity, n the stoichiometric coefficient, CO and BO being a complex and binary oxide. This leads to the following expression for LLZO:Ta ($\text{Li}_{6.45}\text{Al}_{0.05}\text{La}_3\text{Zr}_{1.6}\text{Ta}_{0.4}\text{O}_{12}$):

$$C_{p,m}(\text{LLZO:Ta}) = 3.225C_{p,m}(\text{Li}_2\text{O}) + 0.025C_{p,m}(\text{Al}_2\text{O}_3) + 1.5C_{p,m}(\text{La}_2\text{O}_3) + 1.6C_{p,m}(\text{ZrO}_2) + 0.2C_{p,m}(\text{Ta}_2\text{O}_5) \quad (4)$$

The molar heat capacities of the binary oxides (Li_2O , Al_2O_3 , La_2O_3 , ZrO_2 , Ta_2O_5) can be taken from the NIST database.⁵⁸ The molar heat capacity is converted to the specific heat capacity by division with the molar mass of LLZO:Ta ($M_{\text{LLZO:Ta}} = 873.16 \text{ g mol}^{-1}$). The estimation of $C_{p,m}$ by NKR is most accurate at ambient temperature. However, a first estimate of the temperature dependency of $C_{p,m}$ can be done by taking the temperature-dependent heat capacities of the binary oxides into account. Nonetheless, the accuracy of the estimate is clearly reduced at elevated temperatures.⁵⁶ For the present material LLZO:Ta, the measured C_p and the estimated C_p by NKR (orange line in inset Fig. 4) coincide well at ambient temperature (difference 1.6%). Both values first diverge for rising temperatures (differences up to 14.3%) but start to converge again for elevated temperatures due to a slightly steeper slope of the C_p curve estimated by NKR. Other reported data for the temperature-dependent heat capacity of LLZO in a temperature range from 300–800 K by Il'ina *et al.*⁵⁷ corresponds relatively well with the measurement of the present study (difference of 7%). Differences between the measured C_p and reported data can be related to a varying LLZO substitution, the composition and the exact synthesis method of the sample. The measured values are in excellent agreement with a basic theoretical estimation: assuming a rigorously harmonic crystal lattice approximation, C_p and C_v (constant volume) are identical, and $C_v = 3nk_B$, where n is the number of atoms/ions per volume, and $k_B = 1.38 \times 10^{-23} \text{ J K}^{-1}$ (Boltzmann's constant).⁵⁹ A lattice constant of 1.3 nm of a cubic unit cell leads to a cell volume of 2.2 nm^3 , while the number of atoms/ions is $n = 192$ (24 ions in the sum formula $\text{Li}_7\text{La}_3\text{Zr}_2\text{O}_{12}$, of which 8 are necessary to create the cubic cell with the lattice constant of 1.3 nm). This leads to $C_v = 3.61 \text{ J K}^{-1} \text{ cm}^{-3}$, or – by using a density of 5.2 g cm^{-3} – $C_v = 0.69 \text{ J g}^{-1} \text{ K}^{-1}$ (see Fig. 4).

3.5 Raman spectroscopy

In order to confirm the assumed decomposition of LLZO:Ta which starts in an argon atmosphere around 1500 K, as derived

from DSC measurements (Fig. 4), normalized Raman spectra of LLZO:Ta samples which were heated *ex situ* in ambient atmosphere up to 1473 K and 1773 K (III and IV in Fig. 5a) are compared to the non-heated sample (II in Fig. 5a). The corresponding SEM images of the respective sample surfaces are shown in Fig. 5b. All samples were polished before the measurement to remove surficial Li_2CO_3 . As the decomposition of LLZO is associated with its cubic crystal phase, the presented results for the heating of LLZO:Ta are thought to be conferrable to LLZO:Al. The measured Raman spectra of the unheated LLZO:Al and LLZO:Ta samples (I and II in Fig. 5a) can both be assigned to the expected cubic garnet-phase of LLZO.^{16,44,60} Bands between $100\text{--}150 \text{ cm}^{-1}$ correspond to the vibration of the heavy La cations.⁴⁴ The vibrational modes of LiO_6 octahedra occur between $200\text{--}300 \text{ cm}^{-1}$, while the vibrational modes of LiO_4 tetrahedra appear in the range of $300\text{--}500 \text{ cm}^{-1}$, as it has been shown for several other lithium metal oxides.^{61,62} The bands centered at 650 cm^{-1} correspond to the stretching vibration of ZrO_6 octahedra.^{44,60} The additional bands centered at 740 cm^{-1} which are only present in Ta substituted LLZO spectra can be allocated to the stretching vibration of TaO_6 octahedra.¹⁶

The SEM image of the unheated and polished LLZO:Ta sample (I in Fig. 5b) shows a marbled surface, which is related to the surface topography. Some lower surface areas are still – or again – covered with a thin Li_2CO_3 layer which could not be removed during polishing and which results in a minor Raman signal at 1091 cm^{-1} , due to vibrational modes of CO_3^{2-} .^{49,63} The heat treatment of the sample up to 1473 K did not result in a phase change of the LLZO:Ta, as apparent from the Raman

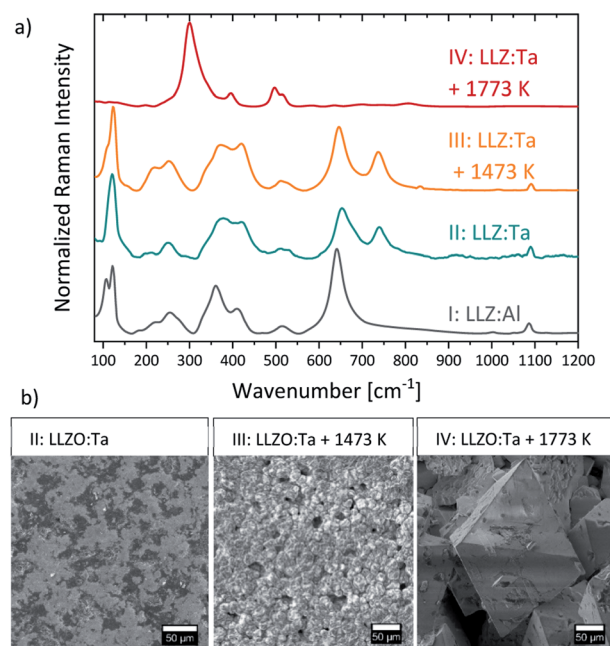


Fig. 5 (a) Raman spectra and (b) corresponding SEM images of (II) polished LLZO:Ta without heat-treatment (III) polished LLZO:Ta heated up to 1473 K and (IV) polished LLZO:Ta heated up to 1773 K (all with 10 kV acceleration voltage).



spectrum of the heated sample (III in Fig. 5a), which is comparable to the unheated sample (II in Fig. 5a). However, despite a comparable Raman signal, SEM measurements revealed a distinct change of the surface morphology (III in Fig. 5b). After heating, the LLZO grains can be recognized individually, as the result of a grain boundary grooving comparable to a thermal etching process.^{29,64} The single LLZO grains are partly covered with a thin Li_2CO_3 layer due to air exposure during cooling, which causes a minor Li_2CO_3 -Raman signal at 1091 cm^{-1} . The heat treatment up to 1773 K led to the decomposition of the highly conductive cubic LLZO phase. The corresponding Raman spectrum (IV in Fig. 5a) shows four major Raman modes at 300 , 395 , 496 , and 513 cm^{-1} , which can be assigned to the pyrochlore $\text{La}_2\text{Zr}_2\text{O}_7$ (LZ) phase.^{65,66} This phase change was verified using SEM imaging, where large characteristic pyrochlore crystal phase octahedral crystals (IV in Fig. 5b) were detected.⁶⁷ The decomposition of LLZO to pyrochlore LZ phase due to lithium loss at elevated temperatures is reported several times in the literature, whereas experimental decomposition temperatures vary in a range from 1523 K (ref. 68) to 1613 K (ref. 23) in air for LLZO without Ta-substitution. Miara *et al.*⁶⁹ predict a theoretical decomposition temperature of 1873 K for LLZO:Ta.

3.6 Laser flash analysis

The thermal conductivity (κ) is the product of thermal diffusivity (α), density (ρ) and specific heat capacity (C_p):

$$\kappa = \alpha \rho C_p \quad (5)$$

The thermal diffusivity can be determined from the LFA measurements employing the procedure introduced by Parker *et al.*³⁴ using a transparent (radiation) model.³⁵ For this experiment the density and temperature-dependent specific heat capacity as described above were considered. For the comparison of LLZO:Ta and LLZO:Al, a porosity correction for κ was done with eqn (6),⁷⁰ which is valid for materials with low emissivity and pore size typical for dense polycrystalline ceramics at temperatures below 1273 K .⁷¹

$$\kappa_s = \frac{\kappa_p}{1 - P_f} \quad (6)$$

With κ_s being the thermal conductivity of the dense solid, κ_p the measured thermal conductivity of the porous material and P_f the pore fraction.

The comparison of LLZO:Ta and LLZO:Al shows a similar progression of their thermal conductivity, which remains relatively constant at similar values for both materials between RT and 900 K at $1.45\text{--}1.55\text{ W m}^{-1}\text{ K}^{-1}$ (Fig. 6). A slight increase for $T > 900\text{ K}$ up to $1.60\text{ W m}^{-1}\text{ K}^{-1}$ is detected, whereas LLZO:Al shows a little larger values. Despite the clearly different grain sizes between LLZO:Ta ($D_{50} = 11.6\text{ }\mu\text{m}$) and LLZO:Al ($D_{50} = 512.5\text{ }\mu\text{m}$), their thermal conductivity is almost similar. This behavior indicates that the phonon scattering at grain boundaries is negligible, which is expected for ceramics above room temperature.⁷¹ The scattering effect of grain boundaries is only

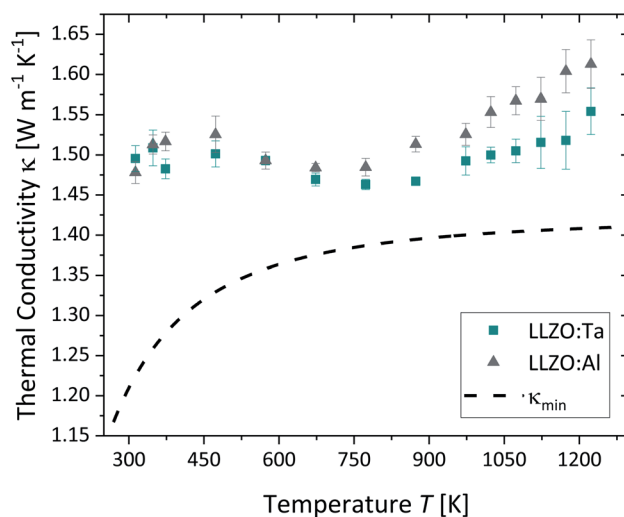


Fig. 6 Temperature dependent thermal conductivity of LLZO:Ta and LLZO:Al (both porosity corrected) determined by laser flash analysis in Ar/H_2 atmosphere. The shown data are the mean of five measurements with standard deviation shown as error bars. κ_{min} is the amorphous limit of the thermal conductivity estimated with eqn (8).

important at low temperatures where the phonon mean free path is comparable to the dimension of the sample.^{71,72}

In a perfect crystal lattice, the thermal resistance would occur due to phonon-phonon interactions, known as Umklapp processes (U-processes).⁷³ At temperatures above the Debye temperature (Θ), the number of U-processes is approximately proportional to the number of phonons, which is then again proportional to the temperature.⁷⁴ At these temperatures, the thermal conductivity is controlled by U-processes and shows a T^{-1} dependency.⁷⁴ In a real crystal, on the other hand, the thermal conductivity is further reduced by phonon scattering at imperfections (such as impurities, vacancies, dislocations, *etc.*) in the crystal lattice. This contribution becomes temperature independent for $T > \Theta$. Overall, the total thermal resistivity can be described as the sum of several thermal resistivities caused by different scattering mechanisms, such as U-processes, scattering at grain boundaries and imperfections. Depending on the considered temperature range, each scattering mechanism contributes differently to the total thermal resistivity.⁷⁴

The LFA measurements in the present study show a relatively constant thermal conductivity of both LLZO for rising temperatures. A possible explanation could be that the phonon mean free path is already in the size range of the interatomic distance in the LLZO crystal lattice, which represents a physically lower limit for the phonon mean free path.^{71,75} The temperature-dependent mean free path of phonons $l(T)$ can be calculated with the following equation:⁷⁵

$$l(T) = \frac{3\kappa(T)}{C_p(T)\rho v} \quad (7)$$

With $\kappa(T)$ being the temperature-dependent thermal conductivity, $C_p(T)$ the temperature-dependent specific heat capacity, ρ the density, and v the velocity of sound in the material. The velocity of sound can be estimated as the square root of the ratio



of bulk modulus and density of a material.⁷⁵ A bulk modulus of approximately 100 GPa is reported in the literature for highly dense LLZO as measured by impulse excitation technique³⁸ and resonant ultrasonic spectroscopy.⁷⁶ This leads to a sound velocity in the order of $v = 4300\text{--}4400\text{ m s}^{-1}$ for LLZO. The insertion of v in eqn (7) yields a phonon mean free path of $3.393\text{--}2.586\text{ \AA}$, which is in the same size range as the bond length of La–O (2.595 \AA) and Zr–O (2.109 \AA).⁷⁷ As the bond length of two atoms represents a physical lower limit for the phonon mean free path, this implies that the phonon mean free path cannot decrease any further for increasing temperatures and becomes constant.^{71,75} This is substantiated using the following amorphous limit (κ_{\min}) consideration. The amorphous limit describes the thermal conductivity for the highest degree of disorder, *i.e.* in the amorphous state. It can be estimated with the following equation developed by Cahill *et al.*:^{78,79}

$$\kappa_{\min} = \left(\frac{\pi}{6}\right)^{1/3} k_B n^{2/3} \sum_i v_i \left(\frac{T}{\Theta_i}\right)^2 \int_0^{\Theta_i/T} \frac{x^3 e^x}{(e^x - 1)^2} dx \quad (8)$$

With k_B being the Boltzmann constant ($1.38 \times 10^{-23}\text{ J K}^{-1}$), n the number of atoms/ions per volume, and the sum is formed over three sound modes (two transverse modes and one longitudinal mode) with the respective speeds of sound v_i and Debye temperatures Θ_i for each polarization (eqn (9)) and T the absolute temperature.⁷⁸

$$\Theta_i = \frac{v_i \hbar (6\pi^2 n)^{1/3}}{k_B} \quad (9)$$

With \hbar being the reduced Planck constant ($1.05 \times 10^{-34}\text{ J s}$). The transverse and longitudinal velocities can be estimated from the shear and Young's modulus, respectively. A shear modulus of $G = 150\text{ GPa}$ and a Young's modulus of $E = 60\text{ GPa}$ are reported in the literature,³⁸ which leads to a transverse velocity of 3592 m s^{-1} and a longitudinal velocity of 5694 m s^{-1} for LLZO. The respective Debye temperatures are calculated with eqn (9) to 478 K and 756 K . The resulting amorphous limit of the thermal conductivity (κ_{\min}) using eqn (8) is plotted as a dashed line in Fig. 6. The measured thermal conductivity is found to be only slightly larger than the amorphous limit (Fig. 6). This means the phonon scattering at inhomogeneities in the crystal lattice is in the same order as expected for the amorphous state, confirming our interpretation. These inhomogeneities in the crystal lattice which act as scattering centers can be occupied and unoccupied Li^+ -sites, as Li^+ -ions show a distorted arrangement the cubic LLZO crystal phase. The substitution with Al or Ta will further create Li-vacancies, which additionally can act as scattering centers (note, Al and Ta, respectively, can be regarded as scattering centers in the same manner). A similar behavior of the thermal conductivity is reported by Wan *et al.*⁸⁰ for the effect of doping of $\text{La}_2\text{Zr}_2\text{O}_7$ with Yb-ions.

The conducted LFA measurements on LLZO show a slight increase in thermal conductivity up to $1.60\text{ W m}^{-1}\text{ K}^{-1}$ for $T > 900\text{ K}$. This is possibly related to further contributions to the thermal conductivity at high temperatures, such as electronic thermal conduction or radiative heat transfer. Yet, a contribution due to an electronic thermal conduction can be considered

negligible for ceramic materials due to their poor electronic conductivity.⁷⁵ However, conductivity by ions could in principle contribute to the overall thermal conductivity such as in electron conductors. The Wiedemann–Franz law⁸¹ is taken into consideration to estimate their potential contribution:

$$\kappa(T) = L\sigma_i(T)T \quad (10)$$

Here L is the Lorenz number ($2.44 \times 10^{-8}\text{ W } \Omega\text{ K}^{-2}$), $\sigma_i(T)$ the temperature-dependent ionic conductivity, and T the absolute temperature. The ionic conductivity is considered to be a thermally activated polaron mechanism. The calculated values are (i) in the range of 0.001 to $0.01\text{ W m}^{-1}\text{ K}^{-1}$, and therefore significantly lower than the measured thermal conductivity values; and (ii) the curvature would not match to the experimental findings. Note that there are different models/Lorenz numbers for the Wiedemann–Franz law, including the Drude-model and the derivation from the Sommerfeld theory, the latter based on the Fermi statistics of spin $\frac{1}{2}$ particles, while Li^+ ions have an integer spin and thus may follow Bose–Einstein statistics. There are Wiedemann–Franz like models published for boson systems, and some deviations of the effective Lorenz number were found, though the Wiedemann–Franz law appeared to be rather robust, even in highly correlated systems. The deviations for L appeared to be less than one order of magnitude. As a general conclusion, the Wiedemann–Franz law can only account for a small part of the overall thermal conductivity in complex oxide systems.^{82–84}

Another contribution to the thermal conductivity could be related to a radiative heat transfer, which means that a certain amount of energy is transmitted by radiation through the material.⁷⁵ The comparison of the detector signals from the LFA measurements, which represent the time-dependent temperature profile at the sample rear surface, reveals first a steplike signal increase followed by the typical time-dependent temperature evolution in LFA measurements (see Fig. S3 in ESI†). The height of this initial step in the detector signal increases for rising temperatures and is more pronounced for LLZO:Al. The steplike signal increase can be interpreted as a radiative heat transport through the sample, which causes an immediate temperature increase at the rear sample surface, and can be fitted with the transparent (radiation) model provided by the LFA manufacturer (NETZSCH LFA Analysis version 7.1.0) (see Fig. S3 in ESI†).³⁵ However, it is thought that the used transparent model cannot fully compensate for the radiative heat contribution. This would lead to an overestimation of the thermal diffusivity, which is the directly derived measurand of the laser flash analysis, and consequently as well of the calculated thermal conductivity. Since the contribution of radiative heat transport increases for rising temperatures, as evident from the larger step height in the detector signal, the derived thermal diffusivity increases as well for temperatures $T > 900\text{ K}$ (see Fig. S4 in ESI†). Furthermore, an increasing standard deviation for each material at every measured temperature is apparent in this temperature range. It is thought that the initial signal step also leads to a reduced LFA-signal quality, as the evaluable signal range between step height and the maximum



of the signal is shortened, which decreases the goodness of fit of the applied transparent model. The thermal conductivity and diffusivity of LLZO:Al is slightly larger than that of LLZO:Ta (Fig. 6 and S4†), which is consistent with a larger step-like increase for the measurement signals of LLZO:Al (see Fig. S3 in ESI†). The higher radiative heat contribution for LLZO:Al might be related to a larger transmission of the laser flash through the sample, due to the significantly reduced number of grain boundaries in the LLZO:Al sample compared to LLZO:Ta.

A reference measurement was conducted to verify the idea that the used transparent fitting model cannot fully compensate for the radiative heat contribution. Therefore, an Al_2O_3 reference sample was measured in Ar- and Ar/ H_2 -atmosphere. The measurements in Ar-atmosphere show a rising step height in the detector signal for $T > 973$ K, which is interpreted as an increasing transmission through the sample by an incremental burning of the carbon coating due to the remaining oxygen in the measurement system (see Fig. S5 in ESI†). No measurements could be evaluated for $T > 1073$ K because the sample was fully transparent for the laser flash as the carbon coating was completely burned. The burning of the carbon coating could be prevented with the reductive Ar/ H_2 -atmosphere and only a minor step can be seen in the detector signals which remains constant for the whole temperature range (see Fig. S5 in ESI†). The derived thermal diffusivity of Al_2O_3 is comparable within the accuracy of measurement in both atmospheres for temperatures up to 1025 K (see Fig. S6 in ESI†). As the step height increases, larger thermal diffusivity values tend to be calculated by the applied transparent model (see inset Fig. S6 in ESI†). Especially for large steps in the detector signal, as apparent for the measurement at 1073 K, the calculated thermal diffusivity is significantly higher (+5.7%) compared to the measurement signal with a small step.

The increase of the thermal diffusivity for LLZO:Ta and LLZO:Al after its minimum at 773–873 K is found to be 3.3% and 5.5%, respectively, which is in the same range as detected for Al_2O_3 (see Fig. S4 in ESI†).

4 Conclusion

Temperature-dependent measurements of the thermal conductivity are discussed for tantalum (Ta)- and aluminum (Al)-substituted LLZO, with both materials showing the highly ion-conductive cubic crystal phase. The effect of the grain size on the thermal conductivity is also considered, as the Al-substitution leads to clearly larger grain sizes when compared to LLZO:Ta. The decomposition of the cubic LLZO phase to pyrochlore $\text{La}_2\text{Zr}_2\text{O}_7$ was found by DSC measurements to happen between 1500 K and 1750 K and was confirmed by Raman and SEM analysis. The temperature-dependent specific heat capacity (C_p) was experimentally determined by the DSC method for LLZO:Ta and can be expressed with the formula $C_p = 0.81 - 2.27 \times 10^{-6} \times T - 2.24 \times 10^{-4} \times T^{-2}$, where T is the absolute temperature. The thermal conductivity (κ) shows a similar progression for LLZO:Ta and LLZO:Al and it remains relatively constant between room temperature and 900 K at $\kappa = 1.45\text{--}1.55 \text{ W m}^{-1} \text{ K}^{-1}$. This behavior indicates, that neither the

substitution-ions (Al or Ta) nor the grain size affects the thermal conductivity. The phonon mean free path was estimated theoretically in this temperature range to be $3.393\text{--}2.586 \text{ \AA}$, which is several orders of magnitude smaller than the grain size. It can therefore be concluded, that the phonon scattering at grain boundaries is negligible for the present material. The estimated phonon mean free path is in the range of the interatomic distance in the LLZO crystal, which represents a physical lower limit for the phonon mean free path. The determined thermal conductivity for LLZO is only slightly larger than the estimated amorphous limit. Both estimates lead to the conclusion that the phonon contribution to the thermal conductivity becomes temperature independent for high temperatures and the main scattering occurs at inhomogeneities in the crystal lattice, such as occupied and unoccupied Li^+ -sites or the substitution ions.

Author contributions

Julian Neises: conceptualization, investigation, validation, writing – original draft, visualization. Walter Sebastian Scheld: conceptualization, investigation, resources, validation, writing – review and editing. Ah-Ram Seok: investigation, resources, validation. Sandra Lobe: conceptualization, resources. Martin Finsterbusch: conceptualization, resources, supervision, funding acquisition. Sven Uhlenbruck: conceptualization, resources, validation, writing – review and editing, supervision. Roland Schmechel: resources. Niels Benson: conceptualization, writing – review and editing, resources, supervision, funding acquisition.

Conflicts of interest

There are no conflicts to declare.

Acknowledgements

This work was funded by the German Federal Ministry for Economic Affairs and Energy (BMWi) as part of the OptiKeraLyt project (FKZ: 03ETE016I) and is gratefully acknowledged here. The authors thank Marie-Theres Gerhards for her help with the DSC measurements and Grit Häuschen for the synthesis and preparation of the LLZO samples.

References

- 1 R. Murugan, V. Thangadurai and W. Weppner, *Angew. Chem., Int. Ed.*, 2007, **46**, 7778–7781.
- 2 V. Thangadurai and W. Weppner, *Adv. Funct. Mater.*, 2005, **15**, 107–112.
- 3 V. Thangadurai and W. Weppner, *J. Am. Ceram. Soc.*, 2005, **88**, 411–418.
- 4 E. J. Cussen, *J. Mater. Chem.*, 2010, **20**, 5167.
- 5 C. A. Geiger, E. Alekseev, B. Lazic, M. Fisch, T. Armbruster, R. Langner, M. Fechtelkord, N. Kim, T. Pettke and W. Weppner, *Inorg. Chem.*, 2011, **50**, 1089–1097.
- 6 J. Awaka, N. Kijima, H. Hayakawa and J. Akimoto, *J. Solid State Chem.*, 2009, **182**, 2046–2052.



- 7 S. Adams and R. P. Rao, *J. Mater. Chem.*, 2012, **22**, 1426–1434.
- 8 J. D. Percival, PhD thesis, University of Surrey, 2009.
- 9 J. L. Allen, J. Wolfenstine, E. Rangasamy and J. Sakamoto, *J. Power Sources*, 2012, **206**, 315–319.
- 10 N. Janani, C. Deviannapoorani, L. Dhivya and R. Murugan, *RSC Adv.*, 2014, **4**, 51228–51238.
- 11 J. Wolfenstine, J. Ratchford, E. Rangasamy, J. Sakamoto and J. L. Allen, *Mater. Chem. Phys.*, 2012, **134**, 571–575.
- 12 Y. Wang and W. Lai, *Electrochem. Solid-State Lett.*, 2012, **15**, A68.
- 13 Y. Li, J. T. Han, C. A. Wang, H. Xie and J. B. Goodenough, *J. Mater. Chem.*, 2012, **22**, 15357–15361.
- 14 L. Dhivya and R. Murugan, *ACS Appl. Mater. Interfaces*, 2014, **6**, 17606–17615.
- 15 S. Ohta, T. Kobayashi and T. Asaoka, *J. Power Sources*, 2011, **196**, 3342–3345.
- 16 T. Thompson, J. Wolfenstine, J. L. Allen, M. Johannes, A. Huq, I. N. David and J. Sakamoto, *J. Mater. Chem. A*, 2014, **2**, 13431–13436.
- 17 Z. Wang, Q. Su, H. Deng and Y. Fu, *ChemElectroChem*, 2015, **2**, 1292–1297.
- 18 X. Huang, T. Xiu, M. E. Badding and Z. Wen, *Ceram. Int.*, 2018, **44**, 5660–5667.
- 19 M. Kotobuki, K. Kanamura, Y. Sato and T. Yoshida, *J. Power Sources*, 2011, **196**, 7750–7754.
- 20 C. Deviannapoorani, S. Ramakumar, N. Janani and R. Murugan, *Solid State Ionics*, 2015, **283**, 123–130.
- 21 K. Tadanaga, R. Takano, T. Ichinose, S. Mori, A. Hayashi and M. Tatsumisago, *Electrochem. Commun.*, 2013, **33**, 51–54.
- 22 Y. Cao, Y.-Q. Li and X.-X. Guo, *Chin. Phys. B*, 2013, **22**, 078201.
- 23 H. Geng, K. Chen, D. Yi, A. Mei, M. Huang, Y. Lin and C. Nan, *Rare Met. Mater. Eng.*, 2016, **45**, 612–616.
- 24 A. Paoletta, W. Zhu, G. Bertoni, S. Savoie, Z. Feng, H. Demers, V. Garipey, G. Girard, E. Rivard, N. Delaporte, A. Guerfi, H. Lorrman, C. George and K. Zaghib, *ACS Appl. Energy Mater.*, 2020, **3**, 3415–3424.
- 25 C. Shuai, P. Feng, C. Gao, Y. Zhou and S. Peng, *Math. Comput. Model. Dyn. Syst.*, 2013, **19**, 1–11.
- 26 R. Bock, M. Onsrud, H. Karoliussen, B. Pollet, F. Seland and O. Burheim, *Energies*, 2020, **13**, 253.
- 27 C. L. Tsai, Q. Ma, C. Dellen, S. Lobe, F. Vondahlen, A. Windmüller, D. Grüner, H. Zheng, S. Uhlenbruck, M. Finsterbusch, F. Tietz, D. Fattakhova-Rohlfing, H. P. Buchkremer and O. Guillon, *Sustain. Energy Fuels*, 2019, **3**, 280–291.
- 28 C. L. Tsai, E. Dashjav, E. M. Hammer, M. Finsterbusch, F. Tietz, S. Uhlenbruck and H. P. Buchkremer, *J. Electroceramics*, 2015, **35**, 25–32.
- 29 W. W. Mullins, *J. Appl. Phys.*, 1957, **28**, 333–339.
- 30 R. E. Chinn, *Ceramography: Preparation and Analysis of Ceramic Microstructures*, ASM International, 2002.
- 31 L. Lutterotti and P. Scardi, *J. Appl. Crystallogr.*, 1990, **23**, 246–252.
- 32 L. Lutterotti, R. Vasin and H.-R. Wenk, *Powder Diffr.*, 2014, **29**, 76–84.
- 33 M. J. O'Neill, *Anal. Chem.*, 1966, **38**, 1331–1336.
- 34 W. J. Parker, R. J. Jenkins, C. P. Butler and G. L. Abbott, *J. Appl. Phys.*, 1961, **32**, 1679–1684.
- 35 H. Mehling, G. Hautzinger, O. Nilsson, J. Fricke, R. Hofmann and O. Hahn, *Int. J. Thermophys.*, 1998, **19**, 941–949.
- 36 Y. Matsuda, A. Sakaida, K. Sugimoto, D. Mori, Y. Takeda, O. Yamamoto and N. Imanishi, *Solid State Ionics*, 2017, **311**, 69–74.
- 37 J. Awaka, A. Takashima, K. Kataoka, N. Kijima, Y. Idemoto and J. Akimoto, *Chem. Lett.*, 2011, **40**, 60–62.
- 38 S. Yu, R. D. Schmidt, R. Garcia-Mendez, E. Herbert, N. J. Dudney, J. B. Wolfenstine, J. Sakamoto and D. J. Siegel, *Chem. Mater.*, 2016, **28**, 197–206.
- 39 Y. Chen, E. Rangasamy, C. R. Dela Cruz, C. Liang and K. An, *J. Mater. Chem. A*, 2015, **3**, 22868–22876.
- 40 N. Janani, S. Ramakumar, S. Kannan and R. Murugan, *J. Am. Ceram. Soc.*, 2015, **98**, 2039–2046.
- 41 R. D. Shannon, *Acta Crystallogr. Sect. A*, 1976, **32**, 751–767.
- 42 C. L. Tsai, V. Roddatis, C. V. Chandran, Q. Ma, S. Uhlenbruck, M. Bram, P. Heitjans and O. Guillon, *ACS Appl. Mater. Interfaces*, 2016, **8**, 10617–10626.
- 43 W. Xia, B. Xu, H. Duan, Y. Guo, H. Kang, H. Li and H. Liu, *ACS Appl. Mater. Interfaces*, 2016, **8**, 5335–5342.
- 44 G. Larraz, A. Orera and M. L. Sanjuán, *J. Mater. Chem. A*, 2013, **1**, 11419–11428.
- 45 Y. Noda and N. Koga, *J. Phys. Chem. C*, 2014, **118**, 5424–5436.
- 46 Y. Ren, H. Deng, R. Chen, Y. Shen, Y. Lin and C. W. Nan, *J. Eur. Ceram. Soc.*, 2015, **35**, 561–572.
- 47 A. Lundblad and B. Bergman, *Solid State Ionics*, 1997, **96**, 173–181.
- 48 R. Ye, C.-L. Tsai, M. Ihrig, S. Sevinc, M. Rosen, E. Dashjav, Y. J. Sohn, E. Figgemeier and M. Finsterbusch, *Green Chem.*, 2020, **22**, 4952–4961.
- 49 W. Xia, B. Xu, H. Duan, X. Tang, Y. Guo, H. Kang, H. Li and H. Liu, *J. Am. Ceram. Soc.*, 2017, **100**, 2832–2839.
- 50 S. Uhlenbruck, C. Dellen, S. Möller, S. Lobe, C. L. Tsai, M. Finsterbusch, M. Bram and O. Guillon, *Solid State Ionics*, 2018, **320**, 259–265.
- 51 S.-M. Hwang, J.-P. Wang and D.-W. Lee, *Metals*, 2019, **9**, 205.
- 52 C. H. P. Lupis, *Chemical Thermodynamics of Materials*, Elsevier Science Publishing Co., Inc, Amsterdam, 1983, pp. 4–6.
- 53 H. Kopp, *Philos. Trans. R. Soc. London*, 1865, **155**, 71–202.
- 54 L. Qiu and M. A. White, *J. Chem. Educ.*, 2001, **78**, 1076.
- 55 J. Leitner, P. Chuchvalec, D. Sedmidubský, A. Strejc and P. Abrman, *Thermochim. Acta*, 2002, **395**, 27–46.
- 56 J. Leitner, P. Voňka, D. Sedmidubský and P. Svoboda, *Thermochim. Acta*, 2010, **497**, 7–13.
- 57 E. A. Il'ina, A. A. Raskovalov and O. G. Reznitskikh, *J. Chem. Thermodyn.*, 2019, **128**, 68–73.
- 58 NIST Chemistry WebBook, SRD 69, <https://webbook.nist.gov/chemistry/form-ser/>, accessed Dezember 2021.
- 59 N. W. Ashcroft and N. D. Mermin, *Solid State Physics*, Saunders College Publishing, New York, 1976, pp. 427–492.
- 60 F. Tietz, T. Wegener, M. T. Gerhards, M. Giarola and G. Mariotto, *Solid State Ionics*, 2013, **230**, 77–82.
- 61 C. Julien, *Ionics*, 2000, **6**, 30–46.



- 62 C. M. Julien and M. Massot, *Mater. Sci. Eng. B*, 2003, **100**, 69–78.
- 63 Y. Li, X. Chen, A. Dolocan, Z. Cui, S. Xin, L. Xue, H. Xu, K. Park and J. B. Goodenough, *J. Am. Chem. Soc.*, 2018, **140**, 6448–6455.
- 64 W. M. Robertson, *J. Am. Ceram. Soc.*, 1981, **64**, 9–13.
- 65 L. Kong, I. Karatchevtseva, D. J. Gregg, M. G. Blackford, R. Holmes and G. Triani, *J. Am. Ceram. Soc.*, 2013, **96**, 935–941.
- 66 Y. Tong, Y. Wang, Z. Yu, X. Wang, X. Yang and L. Lu, *Mater. Lett.*, 2008, **62**, 889–891.
- 67 M. A. Subramanian, G. Aravamudan and G. V. Subba Rao, *Prog. Solid State Chem.*, 1983, **15**, 55–143.
- 68 M. Huang, T. Liu, Y. Deng, H. Geng, Y. Shen, Y. Lin and C.-W. Nan, *Solid State Ionics*, 2011, **204–205**, 41–45.
- 69 L. Miara, A. Windmüller, C. L. Tsai, W. D. Richards, Q. Ma, S. Uhlenbruck, O. Guillon and G. Ceder, *ACS Appl. Mater. Interfaces*, 2016, **8**, 26842–26850.
- 70 J. Franci and W. D. Kingery, *J. Am. Ceram. Soc.*, 1954, **37**, 99–107.
- 71 F. R. Charvat and W. D. Kingery, *J. Am. Ceram. Soc.*, 1957, **40**, 306–315.
- 72 R. Berman, *Contemp. Phys.*, 1973, **14**, 101–117.
- 73 R. Peierls, *Ann. Phys.*, 1929, **395**, 1055–1101.
- 74 D. R. Flynn, in *Mechanical and Thermal Properties of Ceramics*, ed. J. B. J. Wachtman, 1968, pp. 63–113.
- 75 W. D. Kingery, *J. Am. Ceram. Soc.*, 1955, **38**, 251–255.
- 76 J. E. Ni, E. D. Case, J. S. Sakamoto, E. Rangasamy and J. B. Wolfenstine, *J. Mater. Sci.*, 2012, **47**, 7978–7985.
- 77 G. J. Redhammer, G. Tippelt, A. Portenkirchner and D. Rettenwander, *Crystals*, 2021, **11**, 721.
- 78 D. G. Cahill and R. O. Pohl, *Solid State Commun.*, 1989, **70**, 927–930.
- 79 D. G. Cahill, S. K. Watson and R. O. Pohl, *Phys. Rev. B: Condens. Matter Mater. Phys.*, 1992, **46**, 6131–6140.
- 80 C. Wan, W. Zhang, Y. Wang, Z. Qu, A. Du, R. Wu and W. Pan, *Acta Mater.*, 2010, **58**, 6166–6172.
- 81 R. Franz and G. Wiedemann, *Ann. der Phys. und Chemie*, 1853, **165**, 497–531.
- 82 K. K. Lee, A. S. Alexandrov and W. Y. Liang, *Eur. Phys. J. B*, 2004, **39**, 459–468.
- 83 K. Nakata, P. Simon and D. Loss, *Phys. Rev. B*, 2015, **92**, 134425.
- 84 S. Uhlenbruck, B. Büchner, R. Gross, A. Freimuth, A. Maria de Leon Guevara and A. Revcolevschi, *Phys. Rev. B: Condens. Matter Mater. Phys.*, 1998, **57**, R5571–R5574.

